Uncertainty quantification of the transonic flow around the RAE 2822 airfoil

By J. A. S. Witteveen, A. Doostan, R. Pečnik AND G. Iaccarino

1. Motivation and objective

Uncertainty quantification (UQ) is particularly important in transonic flow problems owing to the amplification of input variability across shock waves. In this study we focus on the transonic flow over the RAE 2822 airfoil subject to a combination of uncertainties in the Mach number, angle of attack, and thickness–to–chord ratio. We represent the variability in the form of uniform probability distributions. This problem corresponds to the external flow test case of the *Workshop on Quantification of CFD Uncertainties* (Hirsch *et al.* 2009) organized by the *European Sixth Framework Programme* research project *NODESIM–CFD* on *Non–Deterministic Simulation for CFD–Based Design Methodologies* (Hirsch *et al.* 2006). The test problem poses specific difficulties for UQ methods due to the presence of a discontinuity in the pressure field, although smooth response surfaces for integral quantities of lift, drag, and pitching moment are expected. Two UQ methods are compared to assess their ability to approximate smooth response surfaces in multi–dimensional probability spaces efficiently and to maintain robustness in the presence of discontinuities.

The increased attention for UQ methodologies originates from the experience that conventional methods such as the Monte Carlo approach are too computationally intensive for application to computational fluid dynamics (CFD) problems. On the other hand, the Stochastic Collocation (SC) method (Babuška *et al.* 2007) based on Gauss quadrature sampling and Lagrangian polynomial interpolation in parameter space, although quite efficient, has been shown to have difficulty approximating higher–dimensional probability spaces and discontinuous responses. Also separated solution approximations have been developed to achieve a linear increase of computational costs with dimension (Doostan & Iaccarino 2009), but those are applied only to smooth problems.

For robust approximation of discontinuous responses, multi–element SC (Foo *et al.* 2008) and Stochastic Galerkin (Le Maître *et al.* 2004) methods have been proposed. These approaches are usually based on discretizing the probability space and then using surface reconstruction techniques. For higher–order interpolations these methods can still result in local oscillations and overshoots. Often not all samples in an element can be reused after refinement, and tensor product extensions to higher dimensions are required, which compromises the efficiency of multi–element discretizations.

Motivated by the RAE 2822 test case, we develop in this paper a Simplex Elements Stochastic Collocation (SESC) method that combines a robust approximation of discontinuous responses with an efficient discretization in multi–dimensional probability spaces. The SESC method is an extension of the simplex elements method with Newton–Cotes quadrature (Witteveen *et al.* 2009*a*) to higher order interpolation and randomized sampling. Results are compared with those of the SC method based on Clenshaw–Curtis quadrature. The geometric uncertainty in the thickness–to–chord ratio is treated using a general purpose explicit mesh deformation method based on Inverse Distance Weighting

(IDW) interpolation (Witteveen & Bijl 2009*b*) of the surface displacements to the interior of the spatial grid.

The presentation of the test case results is organized as follows. The SC methods are introduced in section 2. In section 3 the RAE 2822 test case is described. The uncertainty quantification results are presented and compared in section 4. The discussion is concluded by a summary of the future plans in section 5.

2. Stochastic collocation methods

In this section two non–intrusive uncertainty quantification methods are described. The new SESC method is presented in detail, while the standard SC method is only briefly introduced.

2.1. *Simplex elements stochastic collocation*

The SESC method is an extension of the simplex elements discretization of probability space based on Newton–Cotes quadrature (Witteveen *et al.* 2009*a*) to higher order interpolation and randomized sampling. The discretization starts by sampling the vertices of the hypercube probability space and one location in the interior. The simplex elements discretization through the samples is constructed by using a Delaunay triangulation. This triangulation maximizes the minimum angles to avoid skewed simplices by insisting that no sample may lie inside the circumcircle of another simplex. The simplex elements are refined based on the probability contained in the elements, which is its volume in probability space. A location is added randomly in the element with highest probability, but in order to obtain a good spread of the samples the new point is restricted to a sub–simplex of which its vertices are defined by the middle of the $n-1$ faces of the n–simplex. A level two sub–simplex used here for the sampling leads to the example of the discretization of a two–dimensional probability space of Fig. 1.

A piecewise linear interpolation in the elements then satisfies the total variation diminishing (TVD) robustness criterion (Witteveen & Bijl 2009*a*) in probability space. A higher order response surface approximation is constructed using the samples at the vertices of neighboring elements based on a nearest neighbor search. The local polynomials $P_i(\xi)$ in a one–dimensional probability space can be written as

$$P_i(\xi) = \sum_{j=0}^{p} c_{i,j} \Psi_j(\xi), \tag{2.1}$$

for $\xi \in \Xi_i$, $P_i(\xi)$ a polynomial in element Ξ_i of order p, and basis polynomials $\Psi_j(\xi)$ of order j. The polynomial coefficients $c_{i,j}$ can be determined by solving (Hosder *et al.* 2006)

$$\begin{bmatrix} \Psi_0(\xi_{i,0}) & \Psi_1(\xi_{i,0}) & \cdots & \Psi_p(\xi_{i,0}) \\ \Psi_0(\xi_{i,1}) & \Psi_1(\xi_{i,1}) & \cdots & \Psi_p(\xi_{i,1}) \\ \vdots & \vdots & \ddots & \vdots \\ \Psi_0(\xi_{i,p}) & \Psi_1(\xi_{i,p}) & \cdots & \Psi_p(\xi_{i,p}) \end{bmatrix} \begin{pmatrix} c_{i,0} \\ c_{i,1} \\ \vdots \\ c_{i,p} \end{pmatrix} = \begin{pmatrix} v_{i,0} \\ v_{i,0} \\ \vdots \\ v_{i,p} \end{pmatrix}, \tag{2.2}$$

with $v_{i,j} = u(\xi_{i,j})$ the stencil of deterministic samples for element Ξ_i and $\xi_{i,j}$ the corresponding sampling points. The interpolation is made extremum diminishing (ED) by decreasing the polynomial order locally if the interpolant has an extremum in the interior of the element. This is always possible because the piecewise linear interpolation satisfies the ED property by definition. This approach therefore leads to a low–order robust

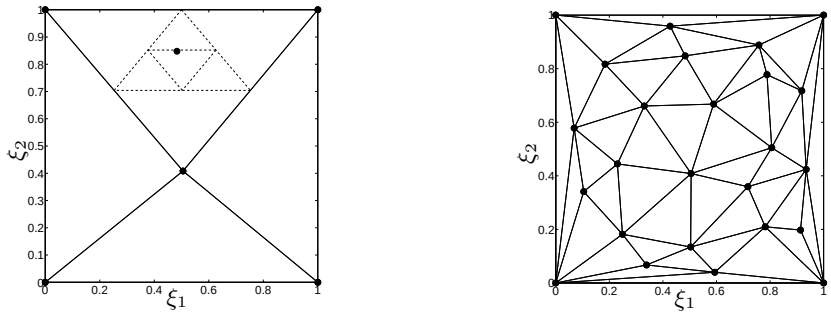

FIGURE 1. SESC discretization of a two–dimensional probability space: (*left*) refinement of the initial mesh and (*right*) the mesh for 25 samples.

approximation of discontinuities and a high–order interpolation for smooth response surfaces. The extremum diminishing property extended to probability space is defined as (Witteveen & Bijl 2009*a*)

$$\min_{\Xi}(w(\boldsymbol{\xi})) \geq \min_{\Xi}(u(\boldsymbol{\xi})) \ \wedge \ \max_{\Xi}(w(\boldsymbol{\xi})) \leq \max_{\Xi}(u(\boldsymbol{\xi})), \tag{2.3}$$

with exact response surface $u(\xi)$ and approximation $w(\xi)$ in the space Ξ of random parameters ξ. The ED concept guaranties that the method generates no unphysical predictions due to overshoots at discontinuities in probability space. In multiple dimensions this robustness property is of particular importance, because it is not trivial to visually inspect the reliability of a multi–dimensional response surface approximation.

This formulation results in high flexibility where an arbitrary number of samples can be used by adding one sample at the time. The polynomial order of the interpolation is also independent of the number of samples for a sufficiently large sample size. For higher dimensional probability spaces the average number of samples per element decreases to a value below one. These properties result in a better scalability of the method with the dimension of probability space compared with tensor product extension of other one-dimensional formulations. The refinement is stopped when a global error convergence criterion is reached. The statistical moments are integrated from the response surface by using Monte Carlo sampling based on the piecewise polynomial approximation, which is fast to evaluate.

2.2. *Stochastic collocation*

The SESC results are compared with those of the tensor product SC method (Babuška *et al.* 2007) based on Clenshaw–Curtis quadrature points. SC uses global polynomial Lagrangian interpolation through the quadrature sampling points to compute integral statistics and probability density functions. The Clenshaw–Curtis abscissas are the extrema of the Chebyshev polynomials in the interval $[-1, 1]$. For any choice of $m > 1$, these points are given by

$$y^j = -\cos\left(\frac{\pi(j-1)}{m-1}\right), \qquad j = 1, \ldots, m, \tag{2.4}$$

which results in a nested rule in the sense that the set of lower–order quadratures abscissas for $m = 2^i + 1$ is a subset of that of a higher–order one with $m = 2^j + 1$ for integer values $i < j$. This hierarchical sampling property allows reusing of the samples when increasing

the order. The tensor product extension of the samples to higher dimensions leads to an exponential increase of the number of samples.

3. Transonic RAE 2822 airfoil

The stochastic test case definition is detailed before discussing the results for the deterministic RAE 2822 verification and validation.

3.1. *Test case description*

The geometry of the RAE 2822 airfoil is described by the design airfoil coordinates tabulated in Cook *et al.* (1979) with a maximal thickness–to–chord ratio of $t/c = 0.1211$. The off–design nominal flow conditions considered here correspond to free stream Mach number $M_\infty = 0.734$, angle of attack $\alpha = 2.79^\mathrm{o}$, and Reynolds number $\mathrm{Re} = 6.5 \cdot 10^6$.

Uncertainties are imposed on the Mach number M_∞, angle of attack α, and thickness–to–chord ratio t/c with standard deviations $\sigma_\mathrm{M} = 0.005$, $\sigma_\alpha = 0.1$, and $\sigma_{\mathrm{t/c}} = 0.005$, respectively, given by independent uniform probability distributions. Results for both uniform and normal input distributions are given in Witteveen *et al.* (2009*b*). These random inputs are selected based on expert opinions of realistic variations in practical operating conditions. The Reynolds number is kept fixed at $\mathrm{Re} = 6.5 \cdot 10^6$ during the stochastic simulations, since different implementations for varying the Mach number M_∞, for example by changing the free stream velocity or the free stream speed of sound, would differently affect the Reynolds number.

The effect of the input variability on the pressure part of the lift C_l, drag C_d, and pitching moment C_m coefficients is represented in terms of the mean, standard deviation, and probability density function. The lift and drag forces are defined as the decomposition of the total aerodynamic pressure force vector perpendicular to and in the direction of the random free stream velocity direction, respectively. The moment reference point coincides with the quarter–chord point. In addition, the mean and uncertainty bars of the surface pressure coefficient C_p, and the mean and standard deviation of the two–dimensional pressure field $p(x, y)$ are computed.

3.2. *Deterministic verification and validation*

The deterministic simulations are based on solving the Reynolds–Averaged Navier–Stokes (RANS) equations on a structured hexahedral C–type mesh using the in–house RANS solver *Joe* (Pečnik *et al.* 2008). A second order spatial discretization is used in combination with the minmod limiter and the Spalart–Allmaras turbulence model. Dual time integration is performed by implicit Euler integration until a convergence criterion of 10^{-5} is reached where the linearized system is solved by the PETSC-GMRES algorithm.

Verification and validation (V&V) of the deterministic RAE 2822 problem is performed for the flow conditions corresponding to case 6 from Cook *et al.* (1979) $M_\infty = 0.725$, $\alpha = 2.92^\mathrm{o}$, and $\mathrm{Re} = 6.5 \cdot 10^6$, which are closest to the mean conditions of the stochastic problem $M_\infty = 0.734$, $\alpha = 2.79^\mathrm{o}$, and $\mathrm{Re} = 6.5 \cdot 10^6$.

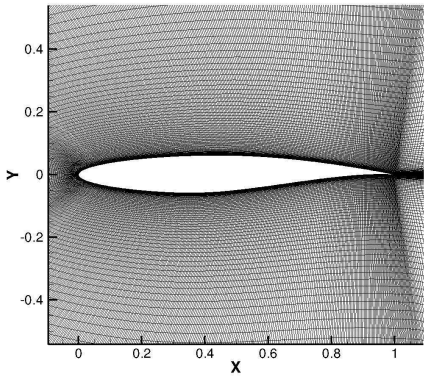

FIGURE 2. Spatial mesh with 112000 volumes.

TABLE 1. Force and moment coefficients for the mean values of the random input.

$M_\infty = 0.734,\ \alpha = 2.79^{\mathrm{o}}$	
C_l	$7.881 \cdot 10^{-1}$
C_d	$6.249 \cdot 10^{-2}$
C_m	$-9.139 \cdot 10^{-2}$

The wind tunnel conditions are corrected for external flow computations in an earlier validation study at NASA (Slater *et al.* 2009) to $M_\infty = 0.729$, $\alpha = 2.31^{\mathrm{o}}$, and $\mathrm{Re} = 6.5 \cdot 10^6$. The latter flow conditions are used for the deterministic V&V study.

The mesh of 112000 volumes shown in Fig. 2 is selected after a mesh convergence study. The deterministic results for the pressure distribution show good agreement with results from the NASA codes *WIND* and *NPARC* available at Slater *et al.* (2009). The validation for the deterministic case is performed by comparing experimental data for case 6 from Cook *et al.* (1979). The surface pressure measurements agree well with the computational data in Fig. 3. The small differences are likely caused by the difference between the design and measured geometry of the airfoil and the correction of the flow conditions for external flow simulations. The pressure field for the mean input values $M_\infty = 0.734$, $\alpha = 2.79^{\mathrm{o}}$ in Fig. 3 shows a shock wave at $x/c = 0.565$. The resulting force and moment coefficients for the mean input are summarized in Table 1. For more results of the deterministic V&V study see Witteveen *et al.* (2009*b*).

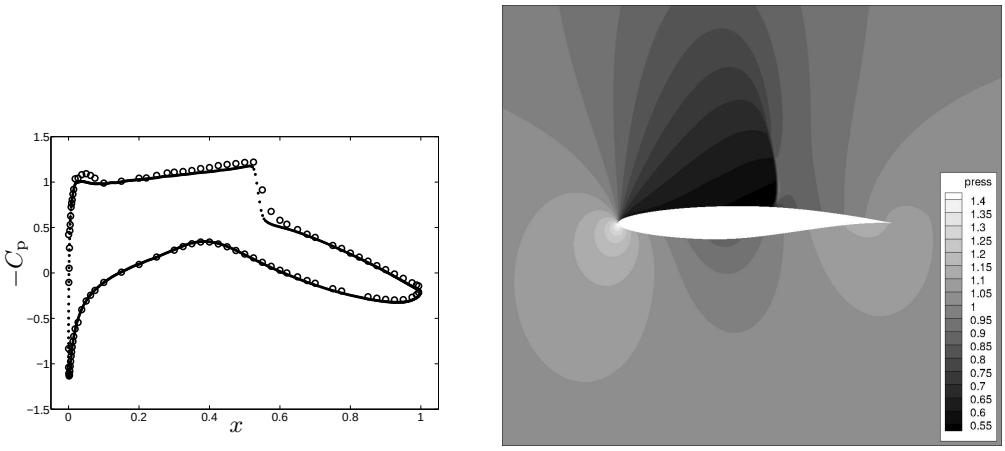

FIGURE 3. Deterministic results: (*left*) validation for case 6 with $M_\infty = 0.729$, $\alpha = 2.31^\circ$ with ($\circ$) experiment and ($\cdot$) computation; (*right*) pressure field (kPa) for mean inputs $M_\infty = 0.734$ and $\alpha = 2.79^\circ$.

4. Results

The mean and standard deviation (st.d.) of the pressure part of the lift C_l, drag C_d, and pitching moment C_m coefficients computed using SESC and SC based on Clenshaw–Curtis quadrature are reported in section 4.1. In section 4.2 the corresponding probability density functions (PDF) are presented. The mean and uncertainty bars of the surface pressure coefficient C_p are compared in section 4.3. Finally in section 4.4 the mean and standard deviation fields of the static pressure are given. The UQ methods are compared with the accuracy of the probabilistic results and the computational costs in terms of the number of deterministic flow solutions required to compute all the statistics of interest.

4.1. *Statistical moments*

The convergence of SESC for the statistical moments of C_l, C_d, and C_m is compared in this section with results of SC. The convergence plot for the statistical moments in Fig. 4 shows the results for SESC up to $n_\mathrm{s} = 100$ samples and for SC up to $n_\mathrm{s} = 125$. Both methods give a fast convergence to comparable values for the statistics of the smooth three–dimensional response surfaces. The results of SESC show its flexibility in the ability to use an arbitrary number of samples while reusing all previous samples. This leads to detailed convergence information in which the noise is caused by the randomized element refinement and small variations in the iteration residuals of the deterministic computations. The SC formulation based on Clenshaw–Curtis quadrature points also reuses all previous samples. However, the fast increase of the number of samples in the nested levels in three dimensions from $n_\mathrm{s} = 1^3$ to $n_\mathrm{s} = 3^3 = 27$ and $n_\mathrm{s} = 5^3 = 125$ results in limited choice of the sampling size.

The values for the statistical moments predicted by SESC and SC are given in Tables 2 and 3, respectively. Table 3 with the results of SC also includes the statistics based on a Clenshaw–Curtis sampling mesh of 9^3 samples, which

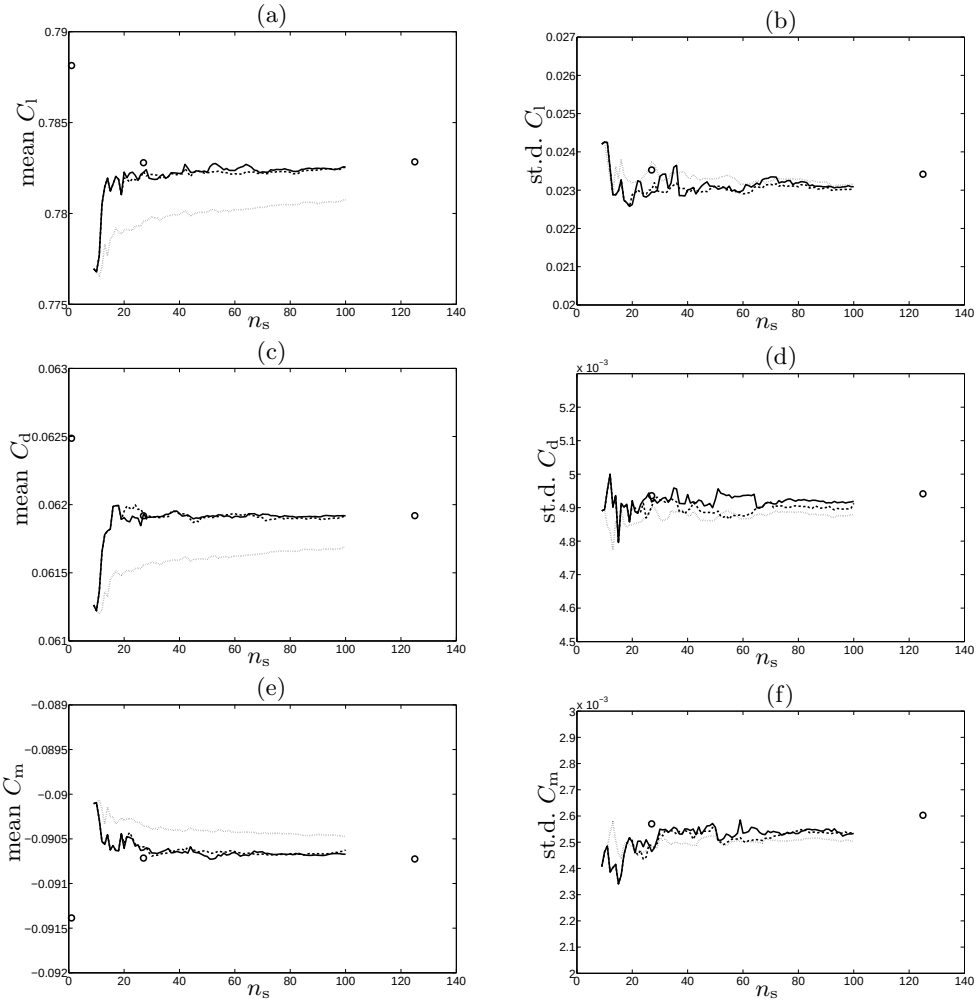

FIGURE 4. Statistical moments of SESC with $(\cdots)$ $p = 1$, (--) $p = 2$, (–) $p = 3$, and $(\circ)$ SC: (*a*) C_l, mean; (*b*) C_l, st.d.; (*c*) C_d, mean; (*d*) C_d, st.d.; (*e*) C_m, mean; (*f*) C_m, st.d.

corresponds to 729 deterministic computations. By comparing the results of SESC for $n_\mathrm{s} = 30$ with those of SC for $n_\mathrm{s} = 27$ it can be seen that SESC and SC show similar convergence behavior in this case. The largest difference between the SESC predictions for $n_\mathrm{s} = 100$ and the SC benchmark result with $n_\mathrm{s} = 729$ is 1.75% for the standard deviation of the pitching moment coefficient.

4.2. *Probability density functions*

The probability densities of C_l, C_d, and C_m give more detailed insight into the effect of the random parameters on the force and moment coefficients. The PDFs of the lift, drag, and moment coefficients are given in Fig. 5. For SESC the results are shown for $n_\mathrm{s} = \{10, 20, 30, 100\}$ samples and SC is considered for $n_\mathrm{s} = \{27, 125, 729\}$ samples. The output PDFs have a clear non–uniform character, which is to be expected from a multi–dimensional uniform input. The results of

TABLE 2. Statistical moments of SESC for the uniform distribution and $p = 3$.

n_s	mean C_l	st.d. C_l	mean C_d	st.d. C_d	mean C_m	st.d. C_m
10	$7.768 \cdot 10^{-1}$	$2.426 \cdot 10^{-2}$	$6.122 \cdot 10^{-2}$	$4.894 \cdot 10^{-3}$	$-9.010 \cdot 10^{-2}$	$2.463 \cdot 10^{-3}$
20	$7.823 \cdot 10^{-1}$	$2.262 \cdot 10^{-2}$	$6.191 \cdot 10^{-2}$	$4.921 \cdot 10^{-3}$	$-9.061 \cdot 10^{-2}$	$2.500 \cdot 10^{-3}$
30	$7.819 \cdot 10^{-1}$	$2.336 \cdot 10^{-2}$	$6.191 \cdot 10^{-2}$	$4.921 \cdot 10^{-3}$	$-9.066 \cdot 10^{-2}$	$2.550 \cdot 10^{-3}$
100	$7.826 \cdot 10^{-1}$	$2.309 \cdot 10^{-2}$	$6.192 \cdot 10^{-2}$	$4.919 \cdot 10^{-3}$	$-9.067 \cdot 10^{-2}$	$2.533 \cdot 10^{-3}$

TABLE 3. Statistical moments of SC for the uniform distribution.

n_s	mean C_l	st.d. C_l	mean C_d	st.d. C_d	mean C_m	st.d. C_m
1	$7.881 \cdot 10^{-1}$	-	$6.249 \cdot 10^{-2}$	-	$-9.139 \cdot 10^{-2}$	-
27	$7.827 \cdot 10^{-1}$	$2.353 \cdot 10^{-2}$	$6.192 \cdot 10^{-2}$	$4.936 \cdot 10^{-3}$	$-9.072 \cdot 10^{-2}$	$2.570 \cdot 10^{-3}$
125	$7.828 \cdot 10^{-1}$	$2.342 \cdot 10^{-2}$	$6.192 \cdot 10^{-2}$	$4.941 \cdot 10^{-3}$	$-9.073 \cdot 10^{-2}$	$2.603 \cdot 10^{-3}$
729	$7.827 \cdot 10^{-1}$	$2.333 \cdot 10^{-2}$	$6.192 \cdot 10^{-2}$	$4.941 \cdot 10^{-3}$	$-9.070 \cdot 10^{-2}$	$2.578 \cdot 10^{-3}$

SESC and SC have a reasonably good agreement. The PDFs of SESC show more variation between the different curves than the SC results, which are practically converged for $n_\mathrm{s} = 27$. SESC gives a significant improvement from $n_\mathrm{s} = 10$ to $n_\mathrm{s} = 20$ samples. Further increasing the number of samples to $n_\mathrm{s} = 30$ and $n_\mathrm{s} = 100$ results only in small differences, except for the moment coefficient C_m.

4.3. *Surface pressure coefficient uncertainty bars*

One of the objectives of UQ is to represent the effect of physical variability in terms of uncertainty bars in the presentation of numerical results similar to the documentation standards for experimental data. The 95% uncertainty bars on the mean C_p of SESC and SC are given in Fig. 6 for a comparable number of samples of $n_\mathrm{s} = 30$ and $n_\mathrm{s} = 27$, respectively. The length of the uncertainty bars is dominated by the surface pressure variations caused by the changing shock wave location. The asymmetric uncertainty bars around the mean in the shock region indicate a strongly nonlinear deformation of the input distributions. The uncertainty bars also show clear local maxima at the leading edge and on the lower surface at the location of maximum airfoil thickness. In the mean sense the discontinuity is smeared out with respect to the deterministic pressure distribution of Fig. 3, owing the varying shock wave location.

The uncertainty bars of SC show small oscillations in the shock region, caused by the global polynomial approximation of the large gradients in the response surface. These overshoots decrease with increasing number of samples, because the weak transonic shock wave does not result in a strong discontinuity at the air-

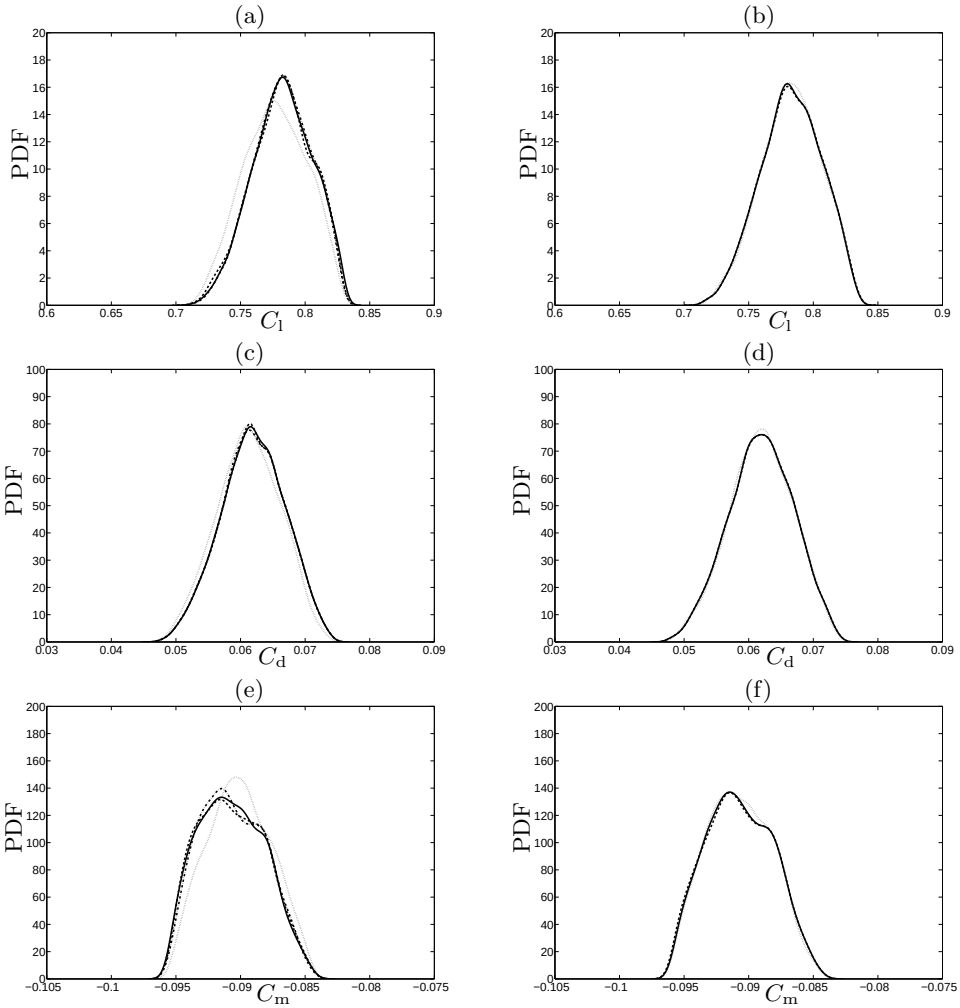

FIGURE 5. Probability density functions of SESC with $(\cdots)$ $n_\mathrm{s} = 10$, (-·-) $n_\mathrm{s} = 20$, (--) $n_\mathrm{s} = 30$, (–) $n_\mathrm{s} = 100$, and SC with $(\cdots)$ $n_\mathrm{s} = 27$, (--) $n_\mathrm{s} = 125$, (–) $n_\mathrm{s} = 729$: (*a*) C_l, SESC; (*b*) C_l, SC; (*c*) C_d, SESC; (*d*) C_d, SC; (*e*) C_m, SESC; (*f*) C_m, SC.

foil surface. The overshoots are absent in the SESC results owing to its extremum diminishing robustness property.

4.4. *Mean and standard deviation pressure field*

Although the integral quantities in problems involving discontinuities can be smooth functions of the random parameters, it is often necessary to compute the mean and standard deviation fields of local flow quantities to understand the mechanism of amplification of input uncertainty. This requires application of the UQ post–processing to the flow quantities in all volumes in the spatial discretization, of which the response surfaces contain a discontinuity in the shock region. Although the geometric uncertainty in the thickness–to–chord ratio t/c is treated by mesh deformation, the volume locations, however, do not coincide

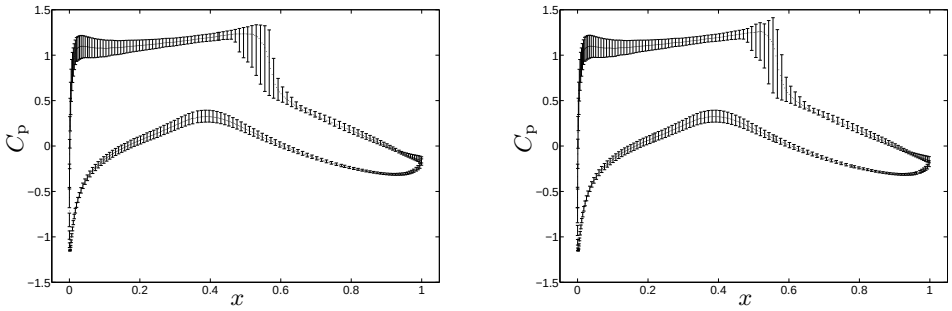

FIGURE 6. Mean surface pressure coefficient C_p and 95% uncertainty bars: (*left*) SESC with $n_s = 30$; (*right*) SC with $n_s = 27$.

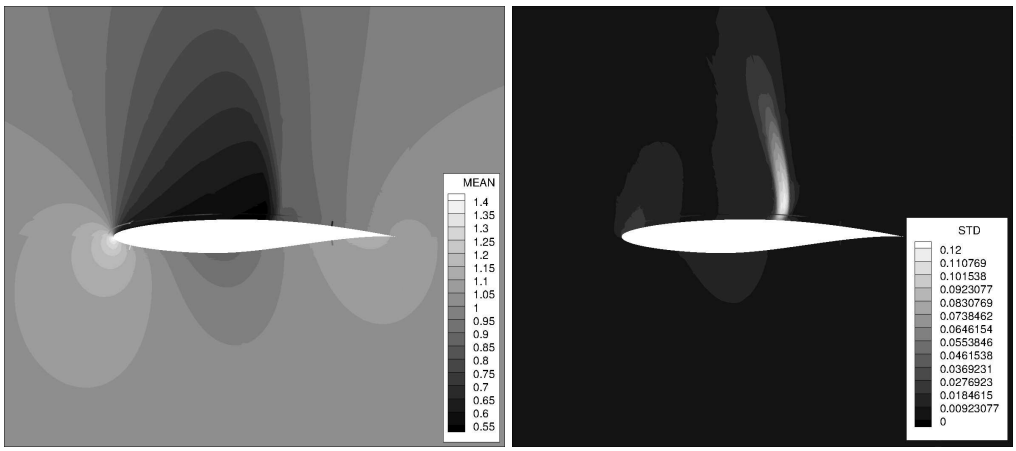

FIGURE 7. Pressure field of SESC for three normal distributions: (*left*) mean; (*right*) standard deviation (kPa).

exactly in physical space for the different samples. The results can be interpret as an approximation of the statistics fields scaled back to the mesh for the mean airfoil thickness. This approach is appropriate here because the small variations in the airfoil thickness slightly affect the contour lines.

SESC with $n_s = 20$ samples is used to generate the mean and standard deviation fields of the static pressure in Fig. 7 for the combination of three normal distributions. The mean pressure field clearly shows the smearing of the shock wave in the mean sense compared with the deterministic pressure solution of Fig. 3. The standard deviation field shows the localized production of standard deviation in the shock region caused by the variation in the shock wave location. The maximum standard deviation is found within the flow field away from the wall owing to the absence of the shock wave in the subsonic boundary layer. This contrasts with earlier findings of a maximum standard deviation at the surface for inviscid Euler computations Witteveen & Bijl (2009*a*). The noise in the contour lines is caused by the post–processing of the mesh partitioning over several processors and other slight mesh imperfections.

5. Future plans

Because of relatively small input uncertainties and the weak transonic shock wave it is difficult to draw specific conclusions from the comparison of SC methods applied to the transonic RAE 2822 airfoil test case of the *NODESIM Workshop on Quantification of CFD Uncertainties*. Simplex Elements Stochastic Collocation is found to combine robustness owing to the extremum diminishing (ED) property with efficiency in higher–dimensional probability spaces. On the basis of nested Clenshaw–Curtis quadrature sampling, SC shows comparable performance with a maximum difference in the standard deviation of C_{m} of 1.75%, however, with limited choice of the sample size and small overshoots in the 95% uncertainty bars for C_{p}.

In future work, more challenging example problems will be considered involving stronger discontinuities and a larger number of random parameters to better distinguish the performance of the compared SC methods. Also validation of uncertainty quantification results will be performed by starting from actually measured physical variations instead of assumed input distributions.

REFERENCES

Babuška, I., Nobile, F. & Tempone, R. 2007 A stochastic collocation method for elliptic partial differential equations with random input data. *SIAM J. Numer. Anal.* **45**, 1005–1034.

Cook, P. H., McDonald, M. A. & Firmin, M. C. P. 1979 Aerofoil RAE 2822 – pressure distributions, and boundary layer and wake measurements. *Experimental Data Base for Computer Program Assessment*, AGARD Report AR 138.

Doostan, A. & Iaccarino, G. 2009 A least–squares approximation of partial differential equations with high–dimensional random inputs. *J. Comput. Phys.* **228**, 4332–4345.

Foo, J., Wan, X. & Karniadakis, G. E. 2008 The multi–element probabilistic collocation method (ME-PCM): Error analysis and applications. *J. Comput. Phys.* **227**, 9572–9595.

Hirsch, Ch. *et al.* 2006 NODESIM–CFD: Non–deterministic simulation for CFD based design methodologies. *European Sixth Framework Programme*, AST5-CT-2006-030959, http://www.nodesim.eu.

Hirsch, Ch. *et al.* 2009 *Workshop on Quantification of CFD Uncertainties.* Vrije Universiteit Brussel, Brussels, Belgium, 29–30 October, http://www.nodesim.eu/workshop.html.

Hosder, S., Walters, R. W. & Perez, R. 2006 A non–intrusive polynomial chaos method for uncertainty propagation in CFD simulations. *44th AIAA Aerospace Sciences Meeting and Exhibit*, Reno, Nevada, AIAA–2006–891.

Le Maître, O. P., Najm, H. N., Ghanem, R. G. & Knio, O. M. 2004 Multi–resolution analysis of Wiener–type uncertainty propagation schemes. *J. Comput. Phys.* **197**, 502–531.

Pečnik, R., Constantine, P., Ham, F. & Iaccarino, G. 2008 A probabilistic framework for high–speed flow simulations. *Annual Research Briefs*, Center for Turbulence Research, Stanford University, 3–17.

Slater, J. W. *et al.* 2009 RAE2822 transonic airfoil, *NPARC Alliance Verification and Validation Archive*, http://www.grc.nasa.gov/WWW/wind/valid/raetaf/raetaf.html.

Witteveen, J. A. S. & Bijl, H. 2009*a* A TVD uncertainty quantification method with bounded error applied to transonic airfoil flutter. *Commun. Comput. Phys.* **6**, 406–432.

Witteveen, J. A. S. & Bijl, H. 2009*b* Explicit mesh deformation using inverse distance weighting interpolation. *19th AIAA Computational Fluid Dynamics Conference*, San Antonio, Texas, AIAA–2009–3996.

Witteveen, J. A. S., Loeven, G. J. A. & Bijl, H. 2009*a* An adaptive stochastic finite elements approach based on Newton–Cotes quadrature in simplex elements. *Comput. Fluids* **38**, 1270–1288.

Witteveen, J. A. S., Doostan, A., Chantrasmi, T., Pečnik, R. & Iaccarino, G. 2009*b* Comparison of stochastic collocation methods for uncertainty quantification of the transonic RAE 2822 airfoil. *Workshop on Quantification of CFD Uncertainties*, Vrije Universiteit Brussel, Brussels, Belgium.